*Environ. Water Eng., 2025, 11(2), 78-88* DOI: 10.22034/ewe.2024.467919.1951

EWE

**Environment and Water Engineering**

**Homepage: www.jewe.ir**

ISSN: 2476-3683

# Photodegradation of methylene blue using silver-doped titanium dioxide nanorods

Mehran Riazian [1]✉, and Sepideh Balasi [1]

[1]Department of Engineering, Faculty of Science, Islamic Azad University, Tonekabon, Iran

**ARTICLE INFO**

**Paper Type:** Research Paper

**Received**: 14 July 2024
**Revised:** 20 September 2024
**Accepted**: 11 November 2024
**Published**: 22 May 2025

**Keywords**
Dopant
Nanostructure
Photodegradation
Sol-Gel
$TiO_2$ Nanorods

***Corresponding author:**
M. Riazian
✉ mehran.riazian@iau.ac.ir

**ABSTRACT**

In this study, to enhance the photocatalytic activity of $TiO_2$ nanorods in the degradation of complex organic pollutants such as textile dyes, the fabrication of the silver-doped $TiO_2$ nanorods in the sol-gel method has been accomplished. To provide optimal conditions for the optical degradation of methylene blue dye, nanostructural and photocatalytic properties of $TiO_2$ nanorods have also been investigated. The crystalline phases, lattice strain and specific surface area of nanoparticles were investigated by the XRD. The morphology of the nanoparticles was analyzed using AFM plus SEM. The FTIR determined the existing chemical bonds. The effect of calcination on the optical properties and the rate of photodegradation of nanorods was studied. The optical bandgap of the nanorods was estimated by the DRS method and verified by the Tauc method. The obtained results showed that nanorods without calcination revealed the smallest crystal size, the highest effective area, the lowest optical band gap, the highest optical degradation rate, and the highest dye removal efficiency. The results indicated that the nanorods were reliable candidates for the degradation of organic pollutants, especially textile dyes.

**How to cite this paper:**
Riazian, M., & Balasi, S. (2025). Photodegradation of methylene blue using silver-doped titanium dioxide nanorods. *Environ. Water Eng.*, *11*(2), 78-88. doi: 10.22034/ewe.2024.467919.1951

## 1. Introduction

Numerous studies have focused on doping $TiO_2$ with various ceramic and transition metals, as well as the fabrication of one-dimensional nanostructures like nanowires, nanotubes, and nanorods, due to their unique properties. These applications include the photocatalytic water-splitting effect (Sajjadizadeh et al., 2024), the photocatalytic effect (Kibria et al., 2024), photovoltaic devices (Khan et al., 2024), and dye-sensitized solar cell electrodes due to their high surface area and *n*-type semiconductor characteristics. Since the discovery of the superhydrophilic photocatalytic property (water contact angle CA < 10°) on the surface of superhydrophilic $TiO_2$, many researchers have focused on utilizing this light-sensitive mechanism by manipulating surface wettability to higher levels in order to achieve greater chemical reactivity, smaller optical bandgap, thermal stability, and more biocompatibility of $TiO_2$ compared to organic and inorganic materials (Abu-Melha, 2024).

Recently, the superhydrophilic capabilities of surfaces have been achieved using the capillary effect of two-dimensional and three-dimensional structures (Kameya and Yabe, 2019). Additionally, dual-functional materials with smart and stimuli-responsive properties that can switch between superhydrophilicity and superhydrophobicity by altering the surface chemistry through changes in surface geometric morphology have been reported (Hao et al., 2024). One-dimensional structures such as nanotubes and nanowires have attracted the attention of many researchers in recent years (Balarabe and Maity, 2024). The $TiO_2$ nanowire, unlike the hydrophilic $TiO_2$ nanoparticle, reveals hydrophobic properties. The methods of synthesizing $TiO_2$ nanorods and nanotubes in the wet method include the transformation of spherical $TiO_2$ particles into tube or rod shapes using strong alkali elements (Riazian, 2017).

Industrial contamination is increasing, with complex organic compounds like azo dyes (with a complex formulation, it has a stable *-N=N- bond* attached to the aromatic system), such as methylene blue, which can pollute water resources. Various methods exist for removing textile dyes, including coagulation, filtration, biological purification, ozonation, and absorption processes. However, these methods have limitations, such as high chemical usage, significant sludge

production, and efficiency constraints. The advanced oxidation process (AOP) is an effective technique for decomposing organic dyes and disinfecting bacteria, utilizing reactive radicals to break down compounds that are resistant to conventional oxidants (Yousefzadeh et al., 2024). Each of the mentioned methods has limitations in execution, such as the use of large quantities of chemicals, the generation of significant amounts of contaminated sludge, operational costs, efficiency issues, and limited applicability. Advanced oxidation processes are effective and reliable methods for the degradation and breakdown of organic dyes in textile industry waste, as well as for disinfecting bacteria (Khalaji, 2024).

This method is based on the photocatalytic degradation of active nanoparticles in an aqueous environment under visible or ultraviolet light irradiation, specifically utilizing semiconductor nanoparticles or transition metals. During this process, photons with sufficient energy can excite the electrons in the valence band of the nanoparticles, transferring them to the conduction band and generating electrons and holes, which in turn produce free radicals. Due to their high reactivity, these generated radicals act as attacking agents on complex carbon structures, degrading them into harmless substances in nature (Manikandan and John, 2020).

The most significant obstacle in the performance of photodegradation is the low rate of production and the high rate of the recombination of electron-hole pairs. Several factors, such as crystal structure, nanoscale properties, morphology, and the size of the synthesized nanoparticles, have a direct impact on the maximum wavelength of absorption ($\lambda_{max}$). The ideal situation is to shift the absorption edge from the ultraviolet region towards longer wavelengths into the visible range ($\lambda_{max} \geq 380$ nm). This transition, known as redshift, enhances the optical-electrical properties and photocatalytic performance of the synthesized nanoparticles (Jin et al., 2022). The photocatalytic efficiency of $TiO_2$ nanoparticles, with a bandgap of approximately 2.9 eV, is limited due to electron-hole recombination (Hamza et al., 2024).

Doping $TiO_2$ nanoparticles with metallic and transition metal nanoparticles, along with utilizing various synthesis methods and precursors, provides a suitable approach to overcome this problem by facilitating the rapid separation of the generated electrons and holes, as well as retarding electron-hole recombination. The photoelectric characteristic of nanoparticles is drastically dependent on the lattice structure so that lattice defects and crystalline phase could alter dislocation density and lattice strain. The strain and stress of the lattice structure are determined by the reliable W-H and H-W methods.

In this study, titanium-doped nanorods were synthesized using a cheap and efficient sol-gel method. The present study investigated the effect of calcination temperature on the nanostructure, optical properties, and photocatalytic activity of the synthesized silver doped nanorods (SDNs) has been investigated in three states without calcination (S1), 300 °C (S2), and 600 °C (S3). The optimal thermal operation for synthesizing SDNs to degrade methylene blue using advanced oxidation processes was determined. The effect of the nanostructure, optical, and physical characteristics of the SDNs on the photocatalytic degradation performance was assessed.

## 2. Materials and Methods

### 2.1 Materials

For the synthesis of the SDNs, the precursors purchased from Merck were utilized. The precursors, ($AgNO_3$, Merck ≥ %99), (TTIP, $Ti(OPr)_4$, Merck ≥ 98%), ($C_2H_5OH$, Merck ≥ 97%), ($HNO_3$, Merck ≥ 65%, 0.1 N) and distilled water are utilized without further purification. The initial solution was prepared by combining (TTIP, distilled water, and $C_2H_5OH$). Then, $AgNO_3$ was dissolved in 20 ml of distilled water and stirred for 48 h at room temperature to obtain a uniform solution with pH = 5. Then, ammonia solution was added drop wisely for sedimentation until pH = 8, and a centrifuge at 1500 rev/min to collect the sediment including doped $TiO_2$. The obtained sediment was dried at 50 °C for 24 h. To form nanorod particles, the powders were stirred in 10 N NaOH solution in a Teflon container for 12 h at 200 °C. Once again, the powders were collected by centrifugation and rinsed with 0.1 N $HNO_3$ and pure distilled water several times to remove sodium ions in the resulting SDNs. Ultimately, the powders were dried in air at 50 °C for 48 h and calcined at two different temperatures (300 and 600 °C). The powders were calcined at a temperature higher than 600 °C, due to the presence of silver ions in the $TiO_2$ matrix, they revealed a great tendency to melt.

### 2.2 Methods and synthesis of the SDNs

The initial solution was prepared by combining TTIP, deionized water, and ethanol. Then, $AgNO_3$ was dissolved in 20 ml of deionized water and stirred for 48 h at room temperature to obtain a uniform solution with a pH = 5. Subsequently, ammonia solution was added dropwise to precipitate the nanoparticles until a pH of 8 was achieved. The resulting precipitate containing the nanoparticles was collected using a centrifuge at 1500 rev/min. The obtained precipitate was dried at 50 °C for 24 h. To fabricate the nanorods, the powders were stirred in a 10 N NaOH solution in a Teflon container for 12 h at 200 °C. The powders were collected again by centrifugation and washed several times with 0.1 N $AgNO_3$ and distilled water to remove sodium ions from the resulting nanoparticles. Finally, the powders were dried in air at 50 °C for 48 h and then calcined at two different temperatures, 300 and 600 °C. The effect of thermal treatment on the synthesis of nanorods was studied by calcining them under three conditions: without calcination (S1), at 300 °C (S2), and at 600 °C (S3). The samples that were calcined at temperatures above 600 °C exhibited a significant tendency to melt due to the presence of silver ions in the titanium oxide matrix. The calcination was carried out to stabilize their crystallinity at temperatures of 300, and 600 °C, with a heating rate of 10 °C/min, an aging time of 2 hours, and cooling at the same rate. All experimental processes were repeated three times, indicating the consistency of the obtained results.

### 2.3 Preparation and instrumentation

The X-ray diffraction was performed using GBC-MMA 007 with a Cu-Kα radiation source at a wavelength of 0.154 nm, with a step size of 0.02° and a scan rate of 10° per minute over a 2θ range from 10 to 80°. To investigate the structure and morphology of the nanorods, CM10 Philips transmission

electron microscope was utilized. To study the morphology and size of the nanoparticles, S-4160 Hitachi field emission scanning electron microscope was employed. To determine of topography and surface analysis of the nanoparticles, an Easy Scan 2 Flex atomic force microscope was used in deionized water with a molar ratio of 1:20 to produce a 0.40% aqueous suspension. To determine the topography and the surface analysis of the nanoparticles, Easy Scan 2 Flex atomic force microscope was used in deionized water with a molar ratio of 1:20 to produce a 0.40% aqueous suspension. To completely separate the nanoparticles, the synthesized nanoparticles were sonicated for 20 *min* using the Sono Swiss SW 40 kHz device. Then, a volume of 50 µm of the diluted solution was placed onto a glass slide that had been cleaned with ethanol and acetone in the ultrasonic device and dried with a nitrogen stream. Atomic Force Microscopy (AFM) analysis of the layer formed at 20 °C and 45% relative humidity was performed using a silicon tip in tapping mode.

### 2.4 Photocatalytic activity and optical band gap of the SDNs

The photocatalytic degradation of methylene blue using the SDNs is indicative of photocatalytic activity. In this experiment, an initial solution of methylene blue dye was prepared at a concentration of 40 ppm. The photocatalytic degradation of methylene blue using the SDNs serves as a measure of photocatalytic activity. In this experiment, a 40 ppm solution of methylene blue dye was initially prepared. Then, it was placed in a dark chamber inside a dark container. The solution was homogenized using an ultrasonic bath for 5 min and stored in a dark place. The concentration of the methylene blue dye solution was determined using a spectrophotometer (VARIAN, UV-Vis 50 Scan) by measuring the absorbance of the sample at a wavelength of 681 nm, based on a calibration curve ($\lambda_{max}$ = 668 nm). The SDNs were then dried in an electric oven at 50 °C for 24 h and subsequently sonicated to completely separate the particles and convert them into a uniform powder. The suspension for the reaction was prepared by creating a stock solution consisting of 0.1 mg of the synthesized nanoparticles in 100 ml of a dye solution containing 40 ppm methylene blue at a pH = 5.5. This mixture was then maintained in a completely dark chamber. Before irradiation, the reaction vessel was homogenized using an ultrasonic device for 5 min in the dark to ensure a proper establishment of the adsorption-desorption equilibrium. During the experiment, the ambient temperature was maintained at 27 ± 1 °C using a small ventilation system. Then, the irradiation reaction of the samples was carried out using two ultraviolet lamps with a wavelength of 253 nm (Philips) and an irradiance of 33.6 µW/cm² at intervals of 10, 20, 30, 40, 50, and 60 min. At the end of each time interval, 10 ml of the stock solution was withdrawn and separated using centrifugation at 6000 rpm. Finally, the solution was filtered through a 0.2 µm filter to remove all photocatalyst particles from the remaining solution. Immediately afterward, the dye solution was selected using a sampler to ensure the absence of nanoparticles, preventing any interference with the absorbance measurements of the solution. Finally, the absorbance spectrum of the filtered solution was measured using a digital spectrophotometer at $\lambda_{max}$ = 668 nm (maximum absorbance) for each sample (Modi et al., 2023; Zhang et al., 2019). Additionally, these steps were repeated for samples S2 and S3.

Various models are utilized to describe and measure the rate of photocatalytic degradation of nanoparticles. The model employed in this research is the Langmuir-Hinshelwood model. This model is applied to describe the reaction rate of the degradation of many organic chemical compounds (Samadi et al., 2019).

$$Ln\frac{C_0}{C} = kt \quad (1)$$

where *C* represents the concentration of dye pollutants at time t in (mg/l), *Co* is the initial concentration of dye before irradiation in (*mg/l*), *k* is the degradation rate constant in (1/min), and *t* is the irradiation time in minutes.

To investigate the optical absorption characteristics and band gap width (Eg) of SDNs, the nanoparticles are first completely dispersed and homogenized in deionized water using an ultrasonic bath at a frequency of 55 kHz for 4 min. Then, the diffuse reflectance spectrum (DRS) of the samples is recorded. An increase in optical absorption in the visible-ultraviolet region indicates more photocatalytic activity of the nanophotocatalysts. The commercial $TiO_2$ sample shows a distinct absorption around 395 nm.

The diffuse reflectance spectrum of the synthesized samples shows a significant optical absorption in the visible region compared to the commercial sample. The band gap width is obtained from the Kobelka-Munk function (Ansari et al., 2016). The Tauc method can also be used to verify the accuracy of the band gap calculations. To investigate the optical band gap, the optical absorption coefficient $\alpha(\lambda)$ is first obtained from Eq. 2 (Zolfaghari et al., 2021a):

$$\alpha(\lambda) = \frac{2.33\,A}{d} \quad (2)$$

where, $\lambda$ stands for the wavelength of the incident photon. The direct and indirect band gaps ($Eg$) of the SDNs are obtained by fitting the reflectance data using the Tauc relation, Eq. 3 (Zolfaghari et al., 2021a):

$$\alpha h\upsilon = A(h\upsilon - E_g)^n \quad (3)$$

where, $\alpha$ is the optical absorption coefficient, $h\upsilon$ is the energy of the incident photon, $A$ is the constant of the relation, and $E_g$ is the optical band gap, which corresponds to the allowed direct or indirect transition depending on the value of $n$ (0.5 or 2), respectively. Longer wavelengths of the UV-visible absorption spectrum reveal a tailing band. This tail arises due to localized energy states in the forbidden band gap, appearing as a tail in the lower energy states. This tail provides important information about potential defects of the holes, crystalline dislocations, and generally the disorder of the crystalline lattice in the synthesized nanoparticles. It is worth mentioning that this tail is known as the Urbach tail, and the corresponding energy is referred to as Urbach energy ($E_u$). The absorption coefficient α behaves exponentially near the absorption edge. The main reason for this exponential behavior is the low degree of crystallinity, point defects, and crystalline imperfections. The relationship between the $\alpha$ and the $E_u$ is given by Eq. 4 (El Mesoudy et al., 2023):

$$Ln(\alpha) = Ln(\alpha_0) + \frac{h\nu}{E_u} \quad (4)$$

where, $\alpha_0$ is a constant, $h\nu$ is the energy of the incident photon, and $E_u$ is the Urbach energy.

### 3. Results and Discussion

The diffraction peaks of the SDNs matched with the peaks available in the databases of X'Pert High Score Plus and Match Crystal Impact (3.8.1.143 64) software. Fig. 1 reveals the formed crystalline phases of the SDNs. The characteristics of the prominent peaks, including 2θ, the interplanar spacing (d-space) from Bragg's equation ($n\lambda = 2d\ sin\theta$), and the size of the crystallites obtained from the Scherrer-Debye equation, are summarized in Table 1. Assuming the spherical shape of the nanocrystallites, the size of the nanocrystallites can be estimated using the Scherrer-Debye method (Galata et al., 2019).

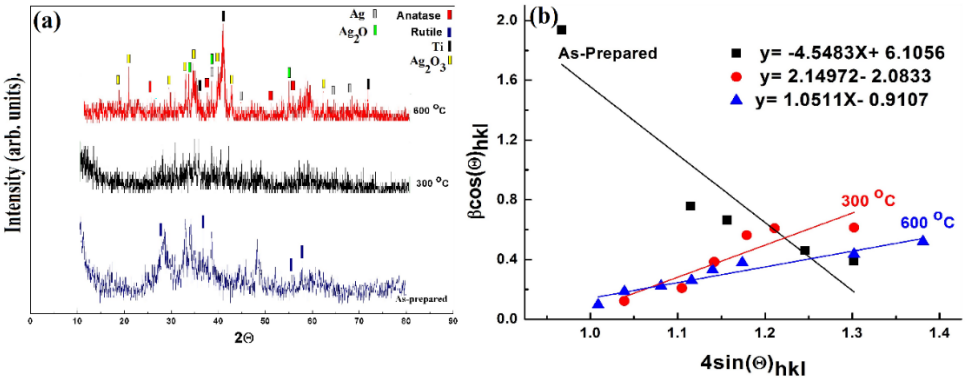


**Fig. 1** :a) The XRD patterns of the SDNs for the as-prepared sample (S1) and b) Relation between $\beta_{hkl}cos\theta$ and 4 $sin\theta$ (Williamson-Hall plots) with different calcination temperatures

**Table 1** Specifications of the XRD peaks: angle, d-space, dislocation density and the size of the nanocrystallite

| Crystallin Phase | As-prepared D(nm) | 2Θ | d(nm) | $\delta \times 10^{16}$ line/m$^2$ | 300 °C D(nm) | d (nm) | 2Θ | $\delta \times 10^{16}$ line/m$^2$ | 600 °C D(nm) | d (nm) | 2Θ | $\delta \times 10^{16}$ line/m |
|---|---|---|---|---|---|---|---|---|---|---|---|---|
| Anatase | 9 | 0.350 | 25.21 | 1.2 | 97 | 0.350 | 25.30 | 0.01 | 102 | 0.353 | 25.26 | 0.009 |
| Rutile | 6 | 0.326 | 27.40 | 2.7 | 24 | 0.322 | 27.50 | 017 | …… | …….. | …….. | …… |
| Ti | 9 | 0.224 | 40.18 | 1.2 | 14 | 0.255 | 40.07 | 0.51 | 19 | 2.28 | 40.23 | 0.277 |
| Ag | 23 | 0.236 | 38.04 | 0.18 | 29 | 0.236 | 38.06 | 0.11 | 142 | 0.236 | 38.07 | 0.005 |
| $Ag_2O$ | 12 | 0.271 | 33.00 | 0.69 | 17 | 0.270 | 33.19 | 0.34 | 33 | 0.270 | 3311 | 0.091 |
| $Ag_2O_3$ | 13 | 0.265 | 33.70 | 0.59 | 15 | 0.268 | 33.30 | 0.40 | 44 | 0.265 | 33.80 | 0.051 |

According to the X-ray data, samples calcined at higher temperatures exhibit higher crystallinity. This is due to the growth of grain boundaries and the strengthening of crystalline nuclei at higher calcination temperatures. The crystalline phases grow with increasing calcination temperature and show larger sizes. This is due to the increase in chemical bond length and the expansion of crystalline planes. Table 1 shows that the rutile crystalline phase is not observed at a calcination temperature of 600 °C. This is due to the phase transformation to the anatase crystalline phase. The synthesis conditions, including the precursors, calcination temperature, laboratory conditions, and the presence of impurities, affect the nucleation of crystallites and the growth of different $TiO_2$ crystalline phases, leading to phase transformation (Theivasanthi and Alagar, 2013).

The dislocation density ($\delta$) of the lattice is obtained from the relation $\delta = \frac{'}{D^2}$, where $D$ is the size of the crystallites in nm. $\delta$ represents the amount of crystalline defects in the structure of the crystallites and is considered as the length of dislocation lines per unit volume of the crystallite (Aghazadeh et al., 2018). Increasing dislocation density has a direct impact on the properties and characteristics of materials. It has been shown that crystallites with high dislocation density are stiffer, and a reduction in crystallite size leads to an increase in dislocation density as well as lattice strain (Theivasanthi & Alagar 2013).

According to Table 1, the dislocation density of the crystalline lattice (line/m²) for all crystalline phases, including the anatase phase, decreased with increasing calcination temperature. The specific surface area (*SSA*) of the nanoparticles was also estimated using *X-ray* diffraction analysis. This is an important photocatalytic characteristic, as it determines prominent features such as adsorption, the heterogeneity of catalysts, and surface reactivity. The SSA and the surface-to-volume ratio (*SA/V*) increased with decreasing particle size (Aghazadeh et al., 2018). The (SSA) and the (SA/V) of the SDNs significantly decreased with increasing calcination temperature.

The Williamson-Hall method was utilized to determine the size of the crystallites and the strain in the lattice. According to the Williamson-Hall method, the broadening of the peaks is due to the contributions from both the size of the crystallites and the lattice strain (Fig. 1). Therefore, the total peak width is considered as a relationship independent of the aforementioned factors and is expressed by the Williamson-Hall equation (Alam et al., 2024).

As shown in Fig.1(b), the lattice strain increased with the increasing calcination temperature. As the calcination temperature increased from the S1 sample (no calcination) to 300 °C, the lattice strain increased from -4.5483 to 2.1497. With further increases in the calcination temperature, the lattice strain decreased to 1.0511. This indicates that with the

increase in calcination temperature, expansion at the crystallite surface occurred and applied tensile stress to the crystalline lattice.

Fig. 2(a-c) shows discrete (island) clusters of SDNs in the flower shape. These discrete regions have completely compact shapes with a length of about 10 µm. After the transformation of the discrete regions into arms, growth continued in a branched or irregular pattern. In this situation, the width of the arms was maintained at about 6 µm. First, at high concentrations, a significant fraction of the guest nanoparticles settled on the host nanoparticles in an island-like formation. These adatom heads could diffuse from the initial island layer and aggregate at the step edges of the same island, resulting in the thickening of the structure. Additionally, as the linear dimensions of these islands increase, a greater percentage of dopant atoms form tree-like branches in the areas between the arms. The $TiO_2$ nanoparticles or the dopant-atoms in these regions tend to fill the empty locations and do not contribute to further radial growth. Radial growth in such areas diminishes to the extent that the islands cannot merge and remain as separate entities. Demerit shapes result from their thermal instability due to kinetic limitations at room temperature (Riazian 2020b).

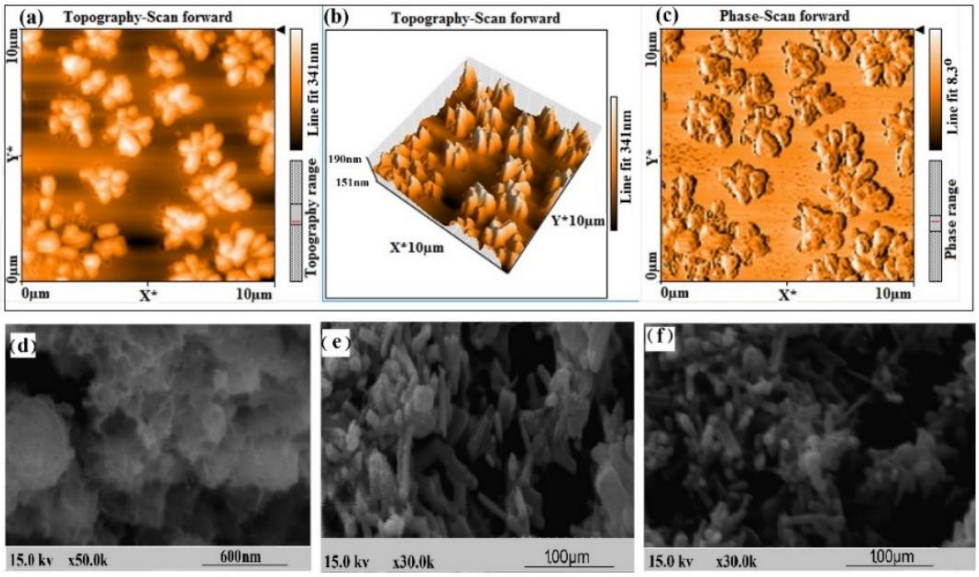


**Fig. 2** AFM morphology of as-prepared doped nanorods : a) 2D scan-forward, b) 3D scan-forward, and c) phase-scan. SEM images of the SDNs calcined at different temperatures: d) as-prepared, e) 300 °C, and f) 600 °C

The surface roughness parameters, such as average roughness $S_a$, median roughness $S_m$, root mean square roughness $S_q$, and maximum peak height (maximum roughness height) from the surface $h_{max}$ are summarized in Table 2 for a section with an area of $10\ \mu m^2$.

**Table 2** Roughness parameters of the *SDNs*

| $S_a$ (nm) | $S_q$ (nm) | $S_m$ (pm) | $h_{max}$ (nm) |
|---|---|---|---|
| 54.15 | 64.90 | 63.48 | 190.00 |

Fig. 2(c, d, e) shows scanning electron microscope images of SDNs. The *S1* has a spherical coating and consists of numerous rods. It appears that the nanoparticles form thin strands in a distinct bundle.

By increasing the calcination temperature, the spherical shells deformed and formed nanorods by overcoming the spherical coating space. Impurities affected the length and shape, elongating the rods and causing separation of the nanorods.

To analyze and investigate the possibility of chemical bond formation between the components of the product, FTIR spectroscopy was employed. Fig. 3 displays the absorption spectra of the powdered samples at various calcination temperatures in the wavenumber range of 400 – 4000 $cm^{-1}$. In the as-prepared sample (*S1*), the bond at 3200 $cm^{-1}$ is attributed to hydroxyl groups from water and ethanol that are trapped in the titania pores. The bending OH bond in the produced gel is observed at 1650 $cm^{-1}$, and slightly lower in energy, the Ti-O bond is visible at 1610 $cm^{-1}$ and 1000 $cm^{-1}$. The peaks at 495 $cm^{-1}$ and 436 $cm^{-1}$ are attributed to the Ti-O-Ti bond. With increasing the calcination temperature, the bending vibrational bands at 3200 and 1650 $cm^{-1}$ diminish in intensity due to the evaporation of the solution.

It is noteworthy that the bandgap width of $TiO_2$ can be modified by doping impurities, including iron, silver, and transition metal atoms. According to Fig. 4, the bandgap energy (*Eg*) is calculated by extrapolating the linear fit of the absorption edge. According to the extrapolated data, the bandgap energies for the S1, S2, and S3 samples are 2.75, 2.84, and 2.98 eV, respectively. It is observed that as the calcination temperature decreases, the size of the nanocrystals and nanorods decreases.

**Fig. 3** FTIR spectra of the SDNs calcined at different temperatures

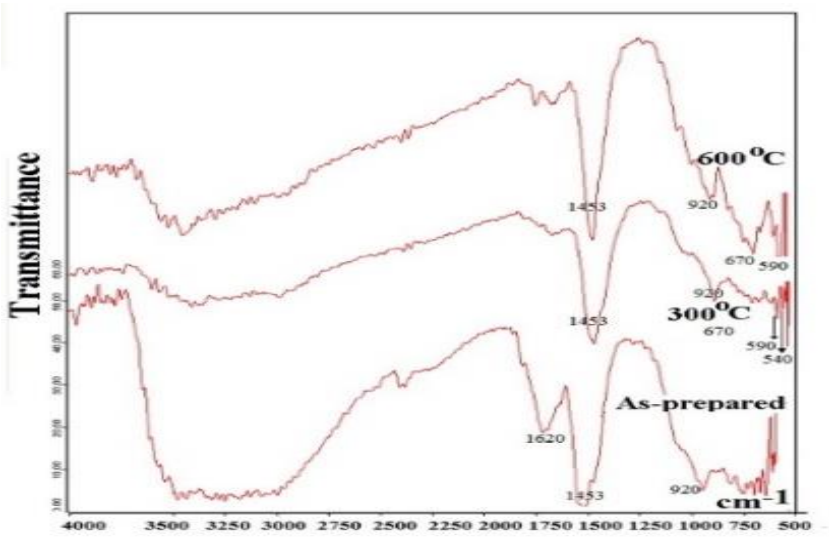


As a result, the quantum size effects, crystallite defects, intrinsic surface states, bonds that substitute electronic states with the bandgap, and the increased chemical-physical reactivity of the nanoparticles lead to greater optical absorption and a smaller bandgap (La Porta et al., 2014). Therefore, the effect of silver doping results in a narrowing of the bandgap and consequently extends the absorption into the visible region.

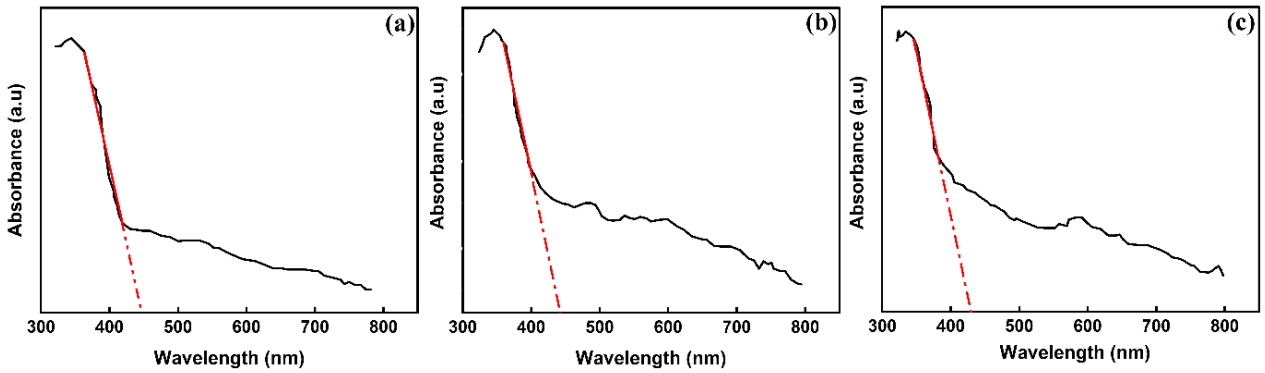


**Fig. 4** The DRS (K-M function) of the *SDNs* calcined at different temperatures: a) S1, b) S2, and c) S3

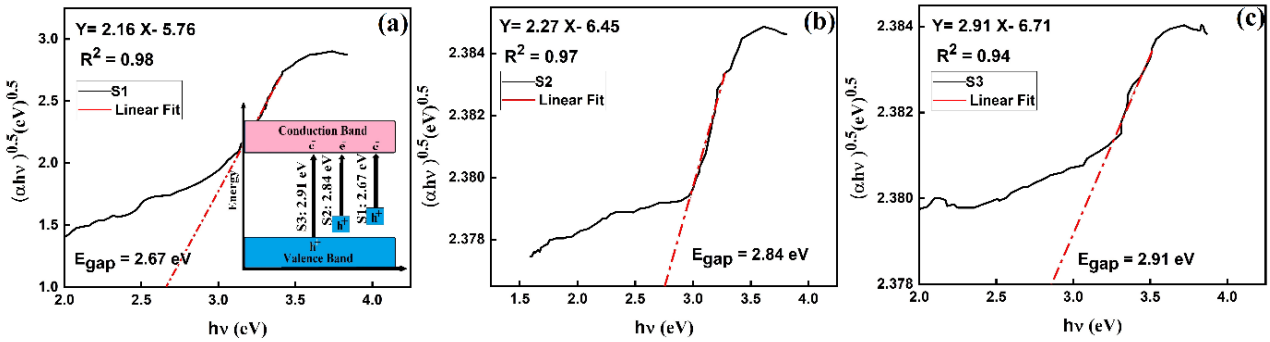


**Fig. 5** the $E_{opt}$ of the Tauc equation from the curve of $(\alpha h\upsilon)^{0.5}$ versus $h\nu$ for the SDNs calcined at different temperatures: a) S1 (Inset: schematic diagram of energy level within the conduction and valence energy bands), b) S2, and c) S3

According to Fig. 5, the bandgap energy is obtained by extrapolating the linear part of the $(\alpha h\upsilon)^{0.5}$ plot against $h\nu$ for the S1, S2, and S3 samples, resulting in values of 2.67, 2.84, and 2.91 eV, respectively. These calculations are consistent with the results obtained from diffuse reflectance spectroscopy spectra and the Kobelka-Munk method. Moreover, the obtained values are lower than the commercial and bulk values (3.2 eV). This reduction is beneficial for increasing the absorption range in photocatalytic activity, as it enables the degradation process to occur by absorbing longer wavelengths or lower energy. The sample *S1* has the lowest optical energy bandgap. Therefore, the increase in the photocatalytic activity of this sample is due to the smaller size and the enhanced effective surface area for photocatalytic interaction. Fig. 5(a) illustrates the bandgap diagram for the synthesized samples in the presence of the valence and conduction bands. The Urbach

energy ($E_u$) can be obtained from the negative inverse slope of the linear fitted graph in Fig 6. The Urbach energy for samples S1, S2, and S3 was calculated to be 0.341, 0.293, and 0.269 eV, respectively. These results indicate that the contribution of crystallite defects, oxygen vacancies, and lattice disorders in the localized states of the S1 is more than that of the S2 and S3. These findings are consistent with the results obtained from X-ray diffraction analysis in determining the density of dislocations, which is an indicator of lattice disorder.

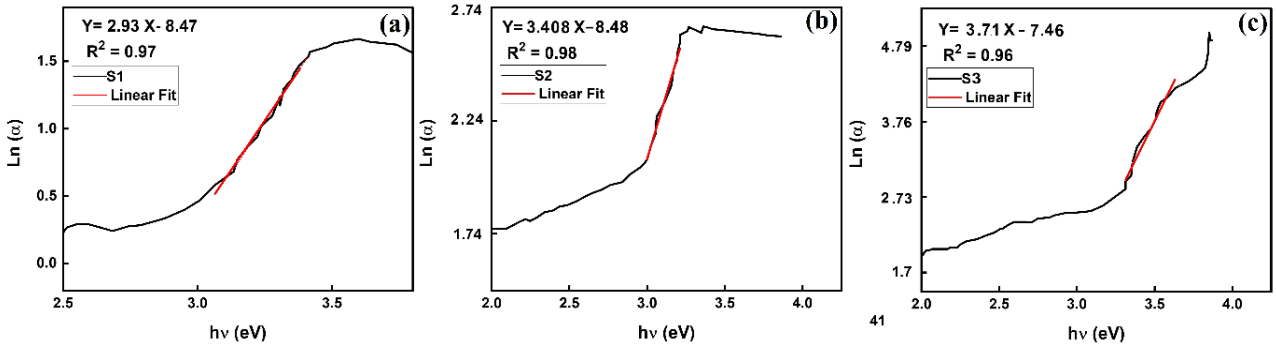


**Fig. 6** The Plot of *Ln(α)* against the hν for determination of the Urbach energy of: a) S1, b) S2, and c) S3

The enhancement of the photocatalytic activity of $TiO_2$ nanorods is due to the expansion of the photochemical response to the visible light region and the delay of electron-hole recombination (Zolfaghari et al., 2021b). In Fig. 7(a), the schematic of the photocatalytic degradation mechanism of the SDNs in an aqueous solution of methylene blue is depicted. Understanding which of the reactive and active radical species plays a greater role in the photocatalytic degradation of pollutants is crucial for selecting nanophotocatalysts. Identifying the key reactive radicals that play a significant role in the photocatalytic degradation of contaminants is crucial for selecting nanophotocatalysts.

To determine the primary role of oxidizing radical species in the photocatalytic degradation mechanism, which includes holes ($h^+$), hydroxyl free radicals ($OH^{\cdot}$), photo-excited electrons (e-), and superoxide radical ions ($\cdot O^{-2}$) during the degradation of methylene blue, a concentration of 0.02 M of specific scavengers, as mentioned below, is utilized. The radical scavengers such as potassium sulfate ($K_2SO_4$), potassium chloride (KCl), potassium bicarbonate (PB), and benzoquinone (BQ) are employed to scavenge electrons, holes, hydroxyl free radicals, and superoxide, respectively (Hamza et al., 2024). The effect of the scavengers in the photocatalytic degradation mechanism is illustrated in Fig. 7.

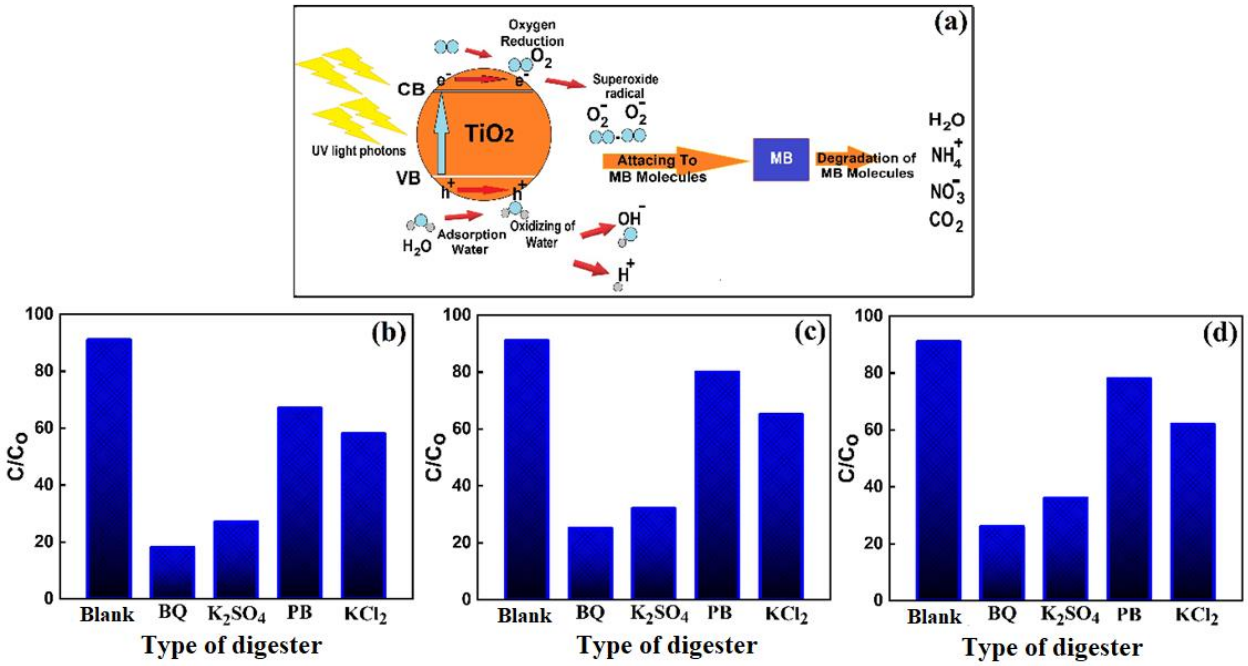


**Fig. 7**: a) Schematic diagram of the photodegradation mechanism for the SDNs. Photodegradation of *MB* by the nanorods alone and in the presence of different radical scavengers for: b) *S1*, c) *S2*, and d) *S3* (Blank: No digester)

In the absence of all scavengers, the concentration of the dyes used was 91%. The results indicate that the photocatalytic degradation of methylene blue dyes in an aqueous solution involving SDNs occurs in the presence of all active radical species, with varying degrees of impact. The influence of the active radicals released during photocatalytic activity is almost the same in all three synthesized samples, with the highest level of degradation attributed to superoxide free radicals, as

indicated by the benzoquinone scavenger. These results indicate that the addition of potassium bicarbonate and potassium chloride, which respectively represent the effects of hydroxyl radicals and the holes generated from photoexcitation, play a minimal role in the degradation mechanism. The primary impact of this degradation is assigned to superoxide free radicals and electrons produced from photoexcitation. Therefore, the primary role of the photocatalytic mechanism is carried out by the reaction $O_2 + e^- \rightarrow \cdot O_2^-$. The mechanism mentioned is the same for all synthesized samples, and the ratio of dye concentrations to the initial concentration follows a consistent pattern in all samples. The photocatalytic degradation activity of the dyes is as follows: BQ > $K_2SO_4$ > $KCl_2$ > PB. The highest reduction in dye concentrations, indicating the most significant impact on the production of superoxide free radicals and electrons generated from photoexcitation, was observed in the S1. This is likely due to the smaller size of the nanorods, which consequently increases the surface-to-volume ratio and enhances the reactivity of this sample compared to the S2 and S3 samples.

The photocatalytic activity of the SDNs is measured by the degradation rate of methylene blue under UV light irradiation. The intensity of the absorption peaks decreases with increasing irradiation time, indicating the photocatalytic degradation of methylene blue dyes. Fig. 8 shows the absorption of methylene blue as a function of irradiation time. This measurement is performed at the maximum absorption wavelength of 668 nm. The intensity of the absorption curves gradually decreases over time due to the photocatalytic degradation of the dyes (Poorarjmand et al., 2018). Fig. 8(a), displays the relative concentration curve (*C/Co*), where C stands the concentration after irradiation time and Co is the initial concentration. Fig. 8-b shows the logarithmic scale of the relative concentration of methylene blue in an aqueous solution (*ln(Co/C)*) as a linear function of UV irradiation time. Figs. 8 (c, d and e) shows the percentage of dye removal as a function of irradiation time. For sample *S1*, the correlation coefficient ($R^2$) is 0.95, and the photocatalytic degradation rate is calculated to be 0.015 $min^{-1}$. After 60 min, 65.75% of the dye was degraded by sample S1, which shows the highest degradation activity compared to the other samples. The sample S3 reveals a lower photocatalytic activity of 0.004 $min^{-1}$, and only 25% of the initial dye concentration was degraded after 60 min UV irradiation.

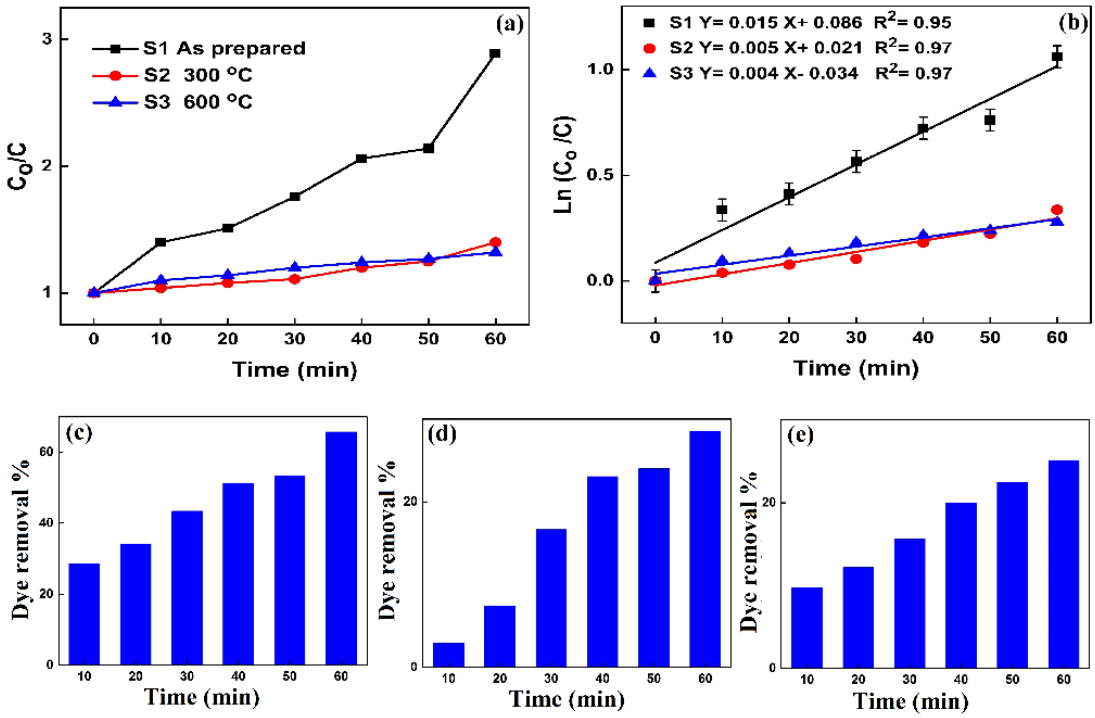


**Fig. 8**: a) Photocatalytic degradation of the *SDNs* versus irradiation time, b) the relation between ln (*Co/C*) and irradiation time for *S1*, *S2*, and *S3*. The dye removal percent versus irradiation time for c) *S1*, d) *S2*, and e) *S3*

All the characteristics of the SDNs are summarized in Table 3. According to this table, the calcination temperature harms the photocatalytic performance quality of the SDNs. By increasing the size and altering the lattice strain, this effect leads to a reduction in the effective surface area of the particles and lattice dislocations, thereby decreasing the efficiency of the nanoparticles in chemical-physical reactions. The bandgap energy of the SDNs has decreased compared with the commercial and bulk samples, and increases with increasing calcination temperature. The dependence of the bandgap energy and Urbach energy on the calcination temperature is quite obvious, as the calcination temperature increases and the Urbach energy decreases, the optical bandgap increases, ultimately leading to a reduction in photocatalytic degradation rate.

**Table 3** Summary of characterization and photodegradation properties of the *SDNs*

| Sample | Calcination temperature | Effective surface area ($m^2/g$) | Ratio of surface area to volume | Dislocation density (line/$m^2$) | Average crystallite size (nm) | Lattice strain | Optical band gap ev | Urbach energy ev | Removal efficiency after 60 min radiation (%) | Photodegradation rate constant (1/min) |
|---|---|---|---|---|---|---|---|---|---|---|
| S1 | As-prepared | 157.604 | 0.666 | $1.23\times10^{16}$ | 9 | -4.54 | 2.67 | 0.341 | 65.75 | 0.015 |
| S2 | 300 ºC | 14.62 | 0.061 | $1.06\times10^{14}$ | 97 | 2.15 | 2.84 | 0.293 | 28.57 | 0.005 |
| S3 | 600 ºC | 13.90 | 0.058 | $9.61\times10^{13}$ | 102 | 1.05 | 2.91 | 0.269 | 25 | 0.004 |

Similar studies recently investigated the optical and photocatalytic properties of $TiO_2$ nanoparticles are summarized in Table 4 alongside the findings of this research. According to Table 4, the SDNs exhibit a small optical bandgap and a significant photocatalytic degradation rate.

**Table 4** Comparison of similar findings concerning *$TiO_2$* nanoparticles with metal and ceramic doping

| Compound | Method of Synthesis | photodegradation rate (1/min) | Optical Band Gap (eV) | (nm) Size | References |
|---|---|---|---|---|---|
| S-Ag-Doped $TiO_2$ Nanorods | Sol-Gel | 0.014-0.022 | 2.87 | 27 | (Riazian, 2020) |
| S-Fe-Doped $TiO_2$ Nanorods | Hydrothermal | 0.019-0.029 | 2.84 | 30-35 | (Zolfaghari et al., 2021b) |
| Fe–S/$TiO_2$@PEG | Sol-Gel | 0.007-0.021 | 2.75-3.21 | 17-20 | (Zolfaghari et al., 2021a) |
| SiO2-Doped $TiO_2$ Nanorods | Sol-Gel | 0.007-0.1 | - | 40-390 | (Riazian, 2017) |
| Al-Doped $TiO_2$ Nanorods | Sol-Gel | 0.04-0.096 | - | 43-400 | (Riazian et al., 2020) |
| $TiO_2$ Nanoparticles | Sol-Gel | 0.008-0.015 | 3.08-3.26 | 20-30 | (Karimi and Graeili 2024) |
| Fe-N -Doped $TiO_2$ Nanorods | Sol-Gel | 0.0016-0.0097 | 2.7-3.1 | 10-14 | (Galata et al., 2019) |

## 4. Conclusion

1. Compared to similar studies, the SDNs demonstrated more efficient photocatalytic activity, establishing them as a suitable candidate for the degradation of the organic dye methylene blue

2. To enhance photocatalytic activity, $TiO_2$ nanorods were synthesized using the sol-gel method with silver doping. Structural analysis revealed by increasing the calcination temperature, the size and lattice strain of the nanorods increased. This indicates that the crystalline surface expanded and experienced thermal stress.

3. The results from scanning electron microscopy and atomic force microscopy indicated that silver impurities affected the length and shape of the nanorods, resulting in increased length and separation from one another. The presence of chemical bonds and the purity of the synthesized products from unwanted compounds were investigated using FTIR spectroscopy.

4. Increasing the calcination temperature caused variations in size and lattice strain, which resulted in a decrease in the effective average surface area and lattice dislocation density of the *SDNs*, consequently reducing the reactivity of the nanoparticles in chemical-physical reactions.

5. To determine the optical band gap, the Kobelka-Munk and Tauc methods estimated values of 2.67, 2.84, and 2.91 *eV* for the *S1*, *S2*, and *S3* samples, respectively. These findings indicated that the reduction in size and the increase in the effective surface area led to a decrease in the band gap and a shift into the visible region.

6. The highest photocatalytic activity was observed in the *S1* sample (without calcination temperature), with a degradation rate of 0.015 $min^{-1}$, and the dye degradation percentage after 60 *min* of irradiation was calculated to be 65.75%.

## Statements and Declarations

### Data availability

The data used or generated in this research are presented in the text of the article.

### Conflicts of interest

The author of this paper declared no conflict of interest regarding the authorship or publication of this paper.

### Author contributions

M. Riazian: validation, project management, formal analysis, and article approval; S. Balasi: resources, data curation, original draft, and article writing.

### References

Abu-Melha, S. (2024). Distinguishable photocatalytic activity of nano polyaniline with quantum dots metal oxide as photocatalysts for photodegradation of Dianix blue dye and different industrial pollutants. *Polyhedron*, *252*, 116781. DOI: 10.1016/j.poly.2023.116781.

Aghazadeh M., & Aghazadeh F. (2018). Green chemistry method with XRD analyzes and absorption of $TiO_2$ nanoparticles modified with use of choline chloride. *Int. J. Bio-Inorg. Hybr. Nanomater*. *7(2)*,97-108.

Alam M. K., Hossain M. S., Bahadur N. M., & Ahmed S. (2024). A comparative study in estimating of crystallite sizes of synthesized and natural hydroxyapatites using Scherrer Method, Williamson-Hall model, Size-Strain Plot and Halder-Wagner Method. *J. Mole. Struct.*, *15(*1306),137820, DOI: 10.1016/j.molstruc.2024.137820

Ansari, S. A., Khan, M. M., Ansari, M. O., & Cho, M. H. (2016). Nitrogen-doped titanium dioxide (N-doped $TiO_2$) for visible light photocatalysis. *New J. Chem.*, *40(4)*, 3000-9. DOI: https://doi.org/10.1039/C5NJ03478G

Balarabe, B. Y., & Maity, P. (2024). A polymer-Au/$TiO_2$ nano-composite based floating catalyst for photocatalytic dye degradation under natural sunlight. *J. Photochem. Photobio. A: Chem.*, *449*, 115405. DOI: 10.1016/j.jphotochem.2023.115405.

El Mesoudy, A., Machon, D., Ruediger, A., Jaouad, A., Alibart, F., Ecoffey, S., & Drouin, D. (2023). Band gap narrowing induced by oxygen vacancies in reactively sputtered $TiO_2$ thin films. *Thin Solid Films*, *769*, 139737. DOI: 10.1016/j.tsf.2023.139737.

Galata, E., Georgakopoulou, E. A., Kassalia, M. E., Papadopoulou-Fermeli, N., & Pavlatou, E. A. (2019). Development of smart composites based on doped-$TiO_2$ nanoparticles with visible light anticancer properties. *Mater.*, *12*(16), 2589. DOI: 10.3390/ma12162589.

Hamza, M. A., El-Sayed, A., El-Shazly, A. N., & Elmahgary, M. G. (2024). Efficient utilization of ceramic waste (cyclone dust waste) for enhancing the photocatalytic performance of $TiO_2$ nanoparticles toward Rhodamine B photodegradation. *J. Clean. Product.*, *434*, 140341. DOI: 10.1016/j.jclepro.2023.140341.

Hao, X., Cheng, Z., Zhang, Y., Xie, J., Zheng, H., Yue, C., & Sheng, W. (2024). Wettability Study of an Acidified Nano-$TiO_2$ Superhydrophobic Surface. *ACS Omega*, *9*(4), 4447-4454. DOI: 10.1021/acsomega.3c07011.

Jin, X., Chen, J., Chen, F., Duan, H., Wang, Z., & Li, J. (2022). Solid-state synthesis of ZnO/ZnS photocatalyst with efficient organic pollutant degradation performance. *Catalyst.*, *12*(9), 981. DOI: 10.3390/catal12090981.

Kameya Y. & Yabe, H. (2019). Optical and superhydrophilic characteristics of $TiO_2$ coating with subwavelength surface structure consisting of spherical nanoparticle aggregates. *Coat. 26*(9), 547. DOI: 10.3390/coatings9090547.

Karimi, M., & Grayeli, A. (2024). Synthesis and characterization of nonmetal-doped $TiO_2$ nanoparticles for photocatalytic degradation of Rhodamine B Dye. *Prog. Color, Colorant. Coat.*, *17*(3), 263-273. DOI: 10.21203/rs.3.rs-3348414/v1.

Khalaji, A. D. (2024). Photodegradation of Bisphenol A using α-$Fe_2O_3$ nanoparticles synthesized by sonochemical assisted. *Nanochem. Res. 9*, 162-71. DOI: 10.22036/ncr.2024.02.008.

Khan, M. I., Hussain, S., Saleem, M., Alzahrani, F. M., Siddique, M., Hassan, M. S., & Iqbal, M. (2024). Enhancing perovskite solar cells: Tailoring the properties of Ti-doped $MAPbBr_3$ for reduced recombination and improved efficiency. *Phys. B: Condens. Matter*, *674*, 415575. DOI: 10.1016/j.physb.2023.415575.

Kibria, M. G., Mohtasim, M. S., Paul, U. K., Das, B. K., & Saidur, R. (2024). Impact of hybrid nano PCM (paraffin wax with $Al_2O_3$ and ZnO nanoparticles) on photovoltaic thermal system: Energy, exergy, exergoeconomic and enviroeconomic analysis. *J. Clean. Product.*, *436*, 140577. DOI: 10.1016/j.jclepro.2024.140577

La Porta, F. A., Andres, J., Li, M. S., Sambrano, J. R., Varela, J. A., & Longo, E. (2014). Zinc blende versus wurtzite ZnS nanoparticles: control of the phase and optical properties by tetrabutylammonium hydroxide. *Phys. Chem. Chem. Phys.*, *16*(37), 20127-20137. DOI: 10.1039/C4CP02611J.

Manikandan, B., & John, R. (2020). Properties of sol-gel synthesized multiphase $TiO_2$ (AB)-ZnO (ZW) semiconductor nanostructure: an effective catalyst for methylene blue dye degradation. *Iran. J. Catal.*, *10*(1), 1-16.

Modi, S., Yadav, V. K, Ali, D, Choudhary, N., Alarifi, S., Sahoo, D. K., Patel, A., & Fulekar, M. H. (2023). Photocatalytic degradation of methylene blue from aqueous solutions by using nano-ZnO/kaolin-clay-based nanocomposite. Water, 15(22), 3915. DOI: https://doi.org/10.3390/w15223915

Poorarjmand, S., Kargar Razi, M., Mahjoob, A. R., & Khosravi, M. (2018). Photocatalytic degradation of Congo Red dye by using nano ZnO and Ni-Co-ZnO nanocomposites. *J. Nanoanal.*, *5*(2), 99-105. DOI: 10.22034/jna.2018.541866.

Riazian, M. (2017). Electrical properties and enhancement of photocatalytic activity of $TiO_2$ nanorods doped with $SiO_2$. *South Africa. J. Chem.*, *70*, 189-199. DOI: 10.17159/0379-4350/2017/v70a26.

Riazian, M. (2020). The increase of the photodegradation and the improvement of the electrical properties of titanate nanorods doped by aluminum oxide and calcination temperature, *Nanomegh.*, *7*(2), 10-18. [In Persian].

Riazian, M., Ashjari, M., & Zolfaghari A. (2020). Photocatalytic degradation, study of optical and nanostructural properties of $TiO_2$ nanoparticles with silver and sulfur dopant in the anatase crystallite phase, *Nano mater. 13*, 46, 71-85. [In Persian].

Sajjadizadeh, H. S., Goharshadi, E. K., & Karimi-Nazarabad, M. (2024). Highly efficient photoanode in visible light water splitting through development of Z-scheme structure between compositing $TiO_2$ with GQDs and Ba doped $VO_2$ (m) with smart selection of Ag nanoparticles sites. *Fuel*, *355*, 129544. DOI: 10.1016/j.fuel.2023.129544.

Samadi, S., Khalili, E., & Allahgholi Ghasri, M. R. (2019). Degradation of methyl red under visible light using N, F-$TiO_2$/$SiO_2$/rGO nanocomposite. *J. Electron. Mater.*, *48*, 12, 7836-7845. DOI: 10.1007/s11664-019-07585-w

Theivasanthi, T., & Alagar, M. (2013). Titanium dioxide ($TiO_2$) nanoparticles XRD analyses: *an insight. arXiv preprint*. *1307*,1091. DOI: 10.48550/arXiv.1307.1091

Yousefzadeh Y, Izadkhah V, Sobhanardakani S, Lorestani B., & Alavinia S. (2024). UiO-66-$NH_2$/guanidine-functionalized chitosan: A new bio-based reusable bifunctional adsorbent for removal of methylene blue from aqueous media. *Int. J. Biol. Macromol.*. *1,254*, 127391. DOI: 10.1016/j.ijbiomac.2023.127391.

Zhang, D., Dai F., Zhang P., An Z., Zhao Y., & Chen L. (2019). The photodegradation of methylene blue in water with PVDF/GO/ZnO composite membrane. *Mater. Sci. Eng.: C. 1(96)*, 684-92. DOI: 10.1016/j.msec.2018.11.049.

Zolfaghari, A., Riazian, M., & Ashjari, M. (2021). Preparation and photodeposition of Fe–S/$TiO_2$@PEG nanoparticles for methylene blue and Evans blue. *Res. Chem. Intermed*., *47*, 1809-1828. DOI: 10.1007/s11164-021-04396-9.

Zolfaghari, A., Riazian, M., & Ashjari, M. (2021). Photodegradation of methylene blue and evans blue by iron and sulphur doped $TiO_2$ nanophotocatalyst under ultraviolet and visible light irradiation. *J. Mexic. Chem. Soc*., *65*(3), 357-375. DOI: 10.29356/jmcs.v65i3.1516.